The Astrophysical Journal, 852:89 (10pp), 2018 January 10 https://doi.org/10.3847/1538-4357/aa9e4c

Late-time Flattening of Type Ia Supernova Light Curves: Constraints from SN 2014J in M82

Yi Yang[1,2], Lifan Wang[1,3], Dietrich Baade[4], Peter. J. Brown[1], Aleksandar Cikota[4], Misty Cracraft[5], Peter A. Höflich[6], Justyn R. Maund[7,10], Ferdinando Patat[4], William B. Sparks[5], Jason Spyromilio[4], Heloise F. Stevance[7], Xiaofeng Wang[8], and J. Craig Wheeler[9]

[1] George P. and Cynthia Woods Mitchell Institute for Fundamental Physics & Astronomy, Texas A. & M. University, Department of Physics and Astronomy, 4242 TAMU, College Station, TX 77843, USA; yi.yang@weizmann.ac.il
[2] Department of Particle Physics and Astrophysics, Weizmann Institute of Science, Rehovot 76100, Israel
[3] Purple Mountain Observatory, Chinese Academy of Sciences, Nanjing 210008, People's Republic of China
[4] European Organisation for Astronomical Research in the Southern Hemisphere (ESO), Karl-Schwarzschild-Str. 2, D-85748 Garching b. München, Germany
[5] Space Telescope Science Institute, Baltimore, MD 21218, USA
[6] Department of Physics, Florida State University, Tallahassee, FL 32306-4350, USA
[7] Department of Physics and Astronomy, University of Sheffield, Hicks Building, Hounsfield Road, Sheffield S3 7RH, UK
[8] Physics Department and Tsinghua Center for Astrophysics (THCA), Tsinghua University, Beijing, 100084, People's Republic of China
[9] Department of Astronomy and McDonald Observatory, The University of Texas at Austin, Austin, TX 78712, USA
Received 2017 March 26; revised 2017 November 21; accepted 2017 November 27; published 2018 January 10

Abstract

The very nearby Type Ia supernova 2014J in M82 offers a rare opportunity to study the physics of thermonuclear supernovae at extremely late phases ($\gtrsim$800 days). Using the *Hubble Space Telescope*, we obtained 6 epochs of high-precision photometry for SN 2014J from 277 days to 1181 days past the *B*-band maximum light. The reprocessing of electrons and X-rays emitted by the radioactive decay chain $^{57}\mathrm{Co} \rightarrow {}^{57}\mathrm{Fe}$ is needed to explain the significant flattening of both the *F*606*W*-band and the pseudo-bolometric light curves. The flattening confirms previous predictions that the late-time evolution of type Ia supernova luminosities requires additional energy input from the decay of ^{57}Co. By assuming the *F*606*W*-band luminosity scales with the bolometric luminosity at $\sim$500 days after the *B*-band maximum light, a mass ratio $^{57}\mathrm{Ni}/^{56}\mathrm{Ni} \sim 0.065^{+0.005}_{-0.004}$ is required. This mass ratio is roughly $\sim$3 times the solar ratio and favors a progenitor white dwarf with a mass near the Chandrasekhar limit. A similar fit using the constructed pseudo-bolometric luminosity gives a mass ratio $^{57}\mathrm{Ni}/^{56}\mathrm{Ni} \sim 0.066^{+0.009}_{-0.008}$. Astrometric tests based on the multi-epoch *HST* ACS/WFC images reveal no significant circumstellar light echoes in between 0.3 and 100 pc from the supernova.

Key words: nuclear reactions, nucleosynthesis, abundances – supernovae: individual (SN 2014J)

1. Introduction

The astronomical community widely agrees that luminous hydrogen-poor Type Ia supernovae (SNe) explosions are powered by the thermonuclear runaway of ($\geqslant$1 $M_\odot$) carbon/oxygen white dwarfs (WDs, Hoyle & Fowler 1960). The accretion-induced explosion fuses $\sim$0.1–1.0 $M_\odot$ of radioactive ^{56}Ni. Type Ia SNe cosmology uses these SNe as the most accurate distance indicators at redshifts out to $z \sim 2$ (Riess et al. 1998; Perlmutter et al. 1999; Riess et al. 2016). Amazingly, this accuracy is achieved without knowing the exact nature of the progenitors.

Prior to maximum luminosity, the light curve of Type Ia SNe is powered by the energy generated by the decay of explosion-synthesized radioactive nuclei. The reprocessing in the ejecta converts the energy to longer wavelengths. The decay chain of $^{56}\mathrm{Ni} \rightarrow {}^{56}\mathrm{Co} \rightarrow {}^{56}\mathrm{Fe}$ provides the main source of energy deposition into the ejecta of Type I SNe (Arnett 1982). During the early phases, the optically thick ejecta trap the energy. The dominant process is Compton scattering of γ-rays produced by the decay $^{56}\mathrm{Ni} + e^- \rightarrow {}^{56}\mathrm{Co} + \gamma + \nu_e$, ($t_{1/2} \sim 6.08$ days), which allows energy to escape as an X-ray continuum or be absorbed by the material in the ejecta via the photoelectric effect (see Milne et al. 1999; Penney & Hoeflich 2014 for comprehensive reviews). The produced ^{56}Co decays to stable ^{56}Fe, and the ^{56}Co decay process, with a half-life $t_{1/2} \sim$ 77 days, dominates after $\sim$200 days, when the expanding ejecta become more and more optically thin, and the column density decreases as t^{-2} (e.g., Arnett 1979; Chan & Lingenfelter 1993; Cappellaro et al. 1997; Milne et al. 1999). Eighty-one percent of the ^{56}Co decays via electron capture ($^{56}\mathrm{Co} + e^- \rightarrow {}^{56}\mathrm{Fe} + \gamma + \nu_e$), and the remainder decays through annihilation of high-energy positrons in the ejecta ($^{56}\mathrm{Co} \rightarrow {}^{56}\mathrm{Fe} + e^+ + \gamma + \nu_e$).

Observations at extremely late phases provide unique opportunities to examine various models exploring the effects of a magnetic field. As long as energy deposition is dominated by positrons being completely trapped by the magnetic field, the slope of the bolometric light curve should match the ^{56}Co decay rate. On the other hand, Milne et al. (1999) suggested a "radially combed" magnetic field, or even a magnetic-field-free situation (as no magnetic field in radial directions will lead to an increasing fraction of positron escape), would cause the light curve to decline faster than the rate of ^{56}Co decay. The discrepancy between the "trapping scenario" with a confining magnetic field and the case without a magnetic field can be as significant as 2 mag in the photometric light curves from 400–800 days (see Figure 9 of Milne et al. 1999). Similar variations of the late-time light curves have been found by Penney & Hoeflich (2014) based on measuring positron transport effects and their dependency on the magnetic field with late-time line profiles. As the SN envelope undergoes homologous expansion, the morphology of the magnetic field

[10] Royal Society Research Fellow.

remains but the Larmor radius increases linearly with time, such that the fraction of escaped photons would exhibit a time-dependence due to the variations of the magnetic field and the light curve should decline faster than the rate of ^{56}Co decay.

Additionally, different effects of nucleosynthesis can be testable through the very late photometric evolution of Type Ia SNe and may be used to discriminate between different explosion models. Two of the most favorable explosion channels: a delayed detonation in a Chandrasekhar-mass WD (Khokhlov 1991) and a violent merger of two carbon-oxygen WDs (Pakmor et al. 2011, 2012), will result in late-time light curves behaving differently due to different amounts of ejecta heating from ^{57}Co and ^{55}Fe (Röpke et al. 2012). The decline rate of the light curve at extremely late times provides a unique opportunity, therefore, to test the enigmatic explosion mechanisms of Type Ia SNe.

Increasing evidence shows the flattening of Type Ia SN light curves around 800–1000 days, i.e., SN 1992A (∼950 days; Cappellaro et al. 1997), SN 2003hv (∼700 days; Leloudas et al. 2009), and SN 2011fe (∼930 days; Kerzendorf et al. 2014). This flattening cannot be explained even by complete trapping of the ^{56}Co positrons. Seitenzahl et al. (2009) suggested that additional heating from the Auger and internal conversion electrons, together with the associated X-ray cascade produced by the decay of $^{57}\mathrm{Co} \rightarrow {}^{57}\mathrm{Fe}$ ($t_{1/2} \approx$ 272 days) and $^{55}\mathrm{Fe} \rightarrow {}^{55}\mathrm{Mn}$ ($t_{1/2} \approx$ 1000 days), will significantly slowdown the decline of the light curve.

Recently, Graur et al. (2016) carried out an analysis of the light curve of SN 2012cg as late as ∼1055 days after the explosion and excluded the scenario in which the light curve of SN 2012cg is solely powered by the radioactive decay chain $^{56}\mathrm{Ni} \rightarrow {}^{56}\mathrm{Co} \rightarrow {}^{56}\mathrm{Fe}$, unless there is an unresolved light echo ∼14 mag fainter than the SN peak luminosity. Another very careful study on the late-time evolution of SN 2011fe has already extended the observing effort to an unprecedented 1622 days past the *B*-band maximum light (Shappee et al. 2016). This analysis has clearly detected the radioactive decay channel powered by ^{57}Co, with a mass ratio of $\log(^{57}\mathrm{Co}/^{56}\mathrm{Co}) = -1.62^{+0.08}_{-0.09}$. This abundance ratio is strongly favored by double degenerate models that require a lower central density. The detection of ^{55}Fe is still unclear at these late epochs (Shappee et al. 2016). Another study based on the pseudo-bolometric light curve for the SN 2011fe has measured the mass ratio of ^{57}Co to ^{56}Co to be 1.3–2.5 times the solar value, which is broadly consistent with the ratios predicted for the delayed-detonation models (Dimitriadis et al. 2017). Additionally, spectroscopic information on the nearby SN 2011fe has been obtained at 981 days (Graham et al. 2015) and 1034 days (Taubenberger et al. 2015). Strong energy input from the radioactive decay of ^{57}Co is required, without which the optical spectrum would be underproduced by a factor of ∼4 (Fransson & Jerkstrand 2015). The produced mass ratio of ^{57}Ni to ^{56}Ni , which gives a strong constraint on the Type Ia SN explosions, is found to be roughly 2.8 and 2 times the solar ratios for SN 2011fe and SN 2012cg, respectively (Fransson & Jerkstrand 2015; Graur et al. 2016).

Recently, Graur et al. (2017) proposed a new model-independent correlation between the stretch of SNe and the shapes of their late-time light curves based on the shapes of the light curve of four type Ia SNe measured at > day 900, i.e., SN 2012cg (Graur et al. 2016), SN 2011fe (Shappee et al. 2016), SN 2014J (this work) and SN 2015F (Graur et al. 2017). They indicated that ^{57}Co may be underproduced in subluminous type Ia SNe. This correlation provides a novel way to test various physical processes driving the slowdown of the type Ia SN light curves ∼900 days after explosion.

SN 2014J was first discovered on January 21.805 UT by Fossey et al. (2014) in the very nearby starburst galaxy M82 (3.53 ± 0.04 Mpc, Dalcanton et al. 2009). Later observations constrained the first light of the SN to January 14.75 UT (Goobar et al. 2014; Zheng et al. 2014). This date is consistent with the early rising recorded by the 0.5 m Antarctic Survey Telescope (AST) during its test observations (Ma et al. 2014), as well as with other pre-discovery limits reported by various groups (Denisenko et al. 2014; Gerke et al. 2014; Itagaki et al. 2014). SN 2014J reached its *B*-band maximum on February 2.0 UT (JD 2,456,690.5) at a magnitude of 11.85 ± 0.02 (Foley et al. 2014). Follow-up photometric and spectroscopic observations have been made by various groups (Lundqvist et al. 2015; Bonanos & Boumis 2016; Srivastav et al. 2016; Johansson et al. 2017). The strength of γ-ray lines (Churazov et al. 2014; Diehl et al. 2015) and an analytic model fit to the pseudo-bolometric light curve (Srivastav et al. 2016) of SN 2014J suggest that ∼0.5–0.6 $M_{\odot}$ of ^{56}Ni was synthesized in the explosion. In this paper, we present our late-time *Hubble Space Telescope* (*HST*) photometric observations of SN 2014J and fit both the *F606W* (broad *V*) band and an estimate of the pseudo-bolometric luminosity evolution with the Bateman equation considering the luminosity contributed by the decay of ^{56}Co, ^{57}Co, and ^{55}Fe. In addition to following a similar approach to that presented in Graur et al. (2016), we provide a careful astrometric analysis of the time evolution of the position and profile of the SN 2014J point source at very late epochs.

2. Observations and Data Reduction

We imaged SN 2014J with the *HST* Advanced Camera for Surveys/Wide Field Channel (*HST* ACS/WFC) during six visits (V1–V6) under multiple *HST* programs: GO-13717 (PI: Wang), GO-14139 (PI: Wang), and GO-14663 (PI: Wang), i.e., V1 ∼ day 277, V2 ∼ day 416, V3 ∼ day 649, V4 ∼ day 796, V5 ∼ day 983, and V6 ∼ day 1181 relative to its *B*-band maximum at a magnitude of 11.85 ± 0.02 on February 2.0 UT (JD 2,456,690.5, Foley et al. 2014). Figure 1 shows the field around SN 2014J. A log of observations is presented in Table 1. Exposures obtained with different ACS visual polarizers and in different filter combinations and visits have been aligned through *Tweakreg* in the *Astrodrizzle* package (Gonzaga et al. 2012).

The throughput of each ACS/WFC polarizer being used by the *Synphot*[11] synthetic photometry does not match the values determined from on-orbit calibrations. We corrected the polarizers' throughput with the values deduced by on-orbit calibrations (i.e., Table 12 of Cracraft & Sparks 2007; also see Biretta et al. 2004). Following the three polarizer cases described in earlier works by Sparks & Axon (1999), we deduced the Stokes vectors from the observations. In this work, we only discuss the observed flux from SN 2014J, and the intensity maps (Stokes *I*) are the only required input parameter

[11] http://www.stsci.edu/institute/software_hardware/stsdas/synphot

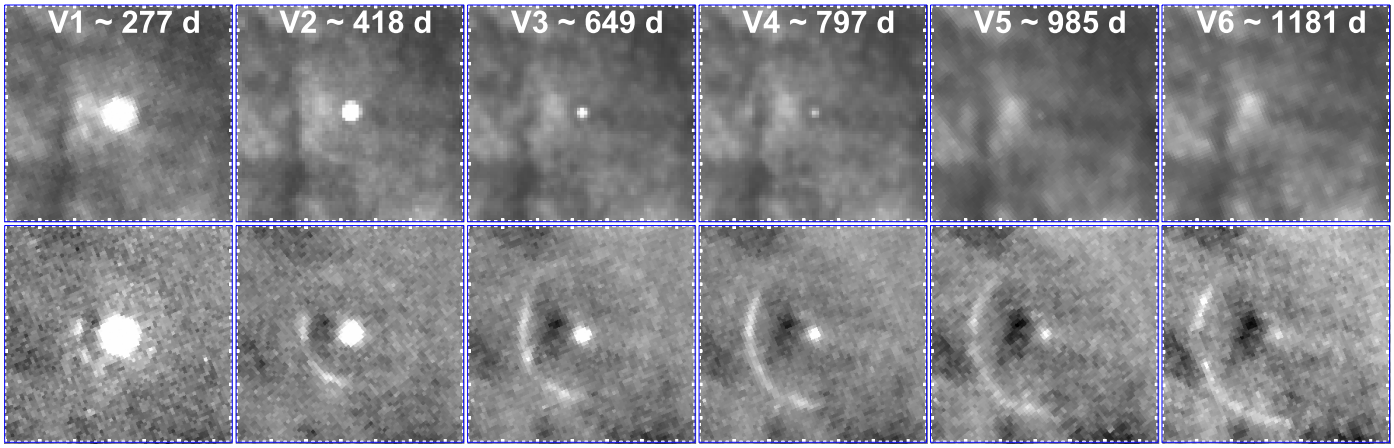

Figure 1. *HST* ACS/WFC *F606W* (upper panels) and associated *F606W*–*F555W* (lower panels) images of SN 2014J obtained in six different visits as labeled. Each square measures 3.″2 = 54 pc along its sides (oriented such that north is up, east is left). The distance between tick marks corresponds to 0.″1. Resolved light echoes arising from interstellar dust clouds are observed at large foreground distances ($\gtrsim$100 pc) from the SN. A luminous arc is visible in the lower left quadrant and a radially diffuse ring can be seen over a wide range in position angle. See Yang et al. (2017) for more details.

for this analysis.

$$I = \frac{2}{3}[r(POL0) + r(POL60) + r(POL120)], \quad (1)$$

where $r(POL0)$, etc. are the count rates in the images obtained through the three polarizers. The polarimetric properties of SN 2014J at different late phases will be discussed in a future work.

After ~600 days past maximum light, the SN became sufficiently dim and the count rates at the central pixels of the SN point-spread function (PSF) became comparable to the bright part of the nebulosity close to the SN. The field shows that the SN lies at one end of a dark lane, and just west of a bright patch of nebulosity. A background subtraction procedure significantly diminishes the time-invariant signals and improves the photometry of evolving faint sources. Unfortunately, we found no pre-SN Hubble images, either with or without the polarizers, showing the same region using filters compatible with our observations. Images obtained on 2006 March 29 (program #10776; PI:Mountain) with *HST* ACS/WFC in the *F435W*, *F555W*, and *F814W* were used as background templates for our *F475W*, *F606W*, and *F775W* exposures, respectively. For each band, the background templates have been scaled and subtracted from the intensity map. The templates have been scaled according to the average flux of four local bright sources [(R.A. = 9:55:40.98, decl. = +69:40:27.16); (R.A. = 9:55:41.99, decl. = +69:40:21.60); (R.A. = 9:55:42.84, decl. = +69:40:31.42); (R.A. = 9:55:43.95, decl. = +69:40:35.47)].

Photometry of SN 2014J was conducted with a circular aperture of 0.″15 (3 pixels in the ACS/WFC FOV) with aperture corrections according to Hartig (2009) and Sirianni et al. (2005). The photometry was performed using the IRAF[12] APPHOT package. The residual of the background was estimated by the median pixel value of an annulus around the SN. Compromising between determining the local background residual with nearby pixels and excluding the contamination from resolved interstellar light echoes (Yang et al. 2017), we choose the inner and outer radii as 1.″2 (24 pixels) and 1.″5 (30 pixels) for V1 and V2, and 0.″45 (9 pixels) and 0.″75 (15 pixels) for V3, V4, V5, and V6. Table 2 presents the AB magnitudes of SN 2014J at the six late epochs.

This photometry strategy has been carried out considering that extremely nonuniform background structures dominate the error budget in the late phases of the SN 2014J photometry, especially after V4. For the scientific consideration of this study, which is testing the models for the light curve evolution at very late phases, the major concern in the data reduction procedure is to obtain the correct decline rate of the SN light curves. We conducted a sanity check to test the reliability of our measurement by performing photometry on differenced images from our observations obtained at different epochs. Observations on V3 ~ day 649 were subtracted from the observations on V4, V5, and V6. This directly measures the differential fluxes and therefore the light curve decline rate. The divergence of magnitude between this estimation and the photometry on scaled and background subtracted images are most significant in V6 when the SN is faintest, which gives ~0.01, 0.04, and 0.05 mag differences in *F475W*, *F606W*, and *F775W*, respectively. This difference is $\lesssim$0.01 in V4 and V5. We conclude that our photometry is reasonable based on the agreement between these two approaches, and the differences represent the systematic uncertainties introduced in the use of subtraction templates acquired with different filters. The photometric uncertainties we quote include this difference, the Poisson noise of the signal, the photon noise of the background, the readout noise contribution (3.75 electrons/pixel for ACS/WFC), and the uncertainties in the aperture corrections. These quantities were added in quadrature. The decline rates between all the epochs, calculated from photometry shown in Table 3 and measured using this sanity check, agree within ~2% and are smaller than the photometric uncertainties.

We correct our measurements for both the interstellar dust extinction in the SN host galaxy and the Galactic extinction toward SN 2014J. In fact, any imperfection in the extinction correction will only affect the individual magnitudes but not the decline rates of the light curves. A peculiar extinction law $R_V \sim 1.4$ toward the SN 2014J line of sight has been suggested by many studies (Amanullah et al. 2014; Foley et al. 2014;

[12] IRAF is distributed by the National Optical Astronomy Observatories, which is operated by the Association of Universities for Research in Astronomy, Inc., under cooperative agreement with the National Science Foundation (NSF).

Table 1
Log of Observations of SN 2014J with *HST* ACS/WFC POLV

Filter	Polarizer	Date (UT)	Exp (s)	Phase[a] (Days)	Date (UT)	Exp (s)	Phase[a] (Days)	Date (UT)	Exp (s)	Phase[a] (Days)
F475W	POL0V	2014 Nov 06	3 × 130	276.5	2015 Mar 25	3 × 400	415.6	2015 Nov 12	4 × 1040	648.5
F475W	POL120V	2014 Nov 06	3 × 130	276.5	2015 Mar 25	3 × 400	415.6	2015 Nov 12	4 × 1040	648.7
F475W	POL60V	2014 Nov 06	3 × 130	276.5	2015 Mar 25	3 × 400	415.7	2015 Nov 12	4 × 1040	648.8
F606W	POL0V	2014 Nov 06	2 × 40	276.6	2015 Mar 27	3 × 60	417.9	2015 Nov 12	4 × 311	649.0
F606W	POL120V	2014 Nov 06	2 × 40	276.6	2015 Mar 27	3 × 60	418.0	2015 Nov 13	4 × 311	649.0
F606W	POL60V	2014 Nov 06	2 × 40	276.6	2015 Mar 27	3 × 60	418.0	2015 Nov 13	4 × 311	649.1
F775W	POL0V	2014 Nov 06	2 × 30	276.6	2015 Mar 27	3 × 20	418.0	2015 Nov 12	4 × 100	648.5
F775W	POL120V	2014 Nov 06	1 × 55	276.6	2015 Mar 27	3 × 20	418.0	2015 Nov 12	4 × 100	648.7
F775W	POL60V	2014 Nov 06	1 × 55	276.6	2015 Mar 27	3 × 20	418.0	2015 Nov 12	4 × 100	648.9
F475W	POL0V	2016 Apr 08	4 × 1040	796.2	2016 Oct 12	4 × 1040	983.1	2017 Apr 28	4 × 1040	1181.3
F475W	POL120V	2016 Apr 08	4 × 1040	796.4	2016 Oct 12	4 × 1040	983.3	2017 Apr 28	4 × 1040	1181.4
F475W	POL60V	2016 Apr 08	4 × 1040	796.6	2016 Oct 12	4 × 1040	983.4	2017 Apr 28	4 × 1040	1181.5
F606W	POL0V	2016 Apr 08	4 × 311	796.8	2016 Oct 14	3 × 360	985.1	2017 Apr 28	3 × 360	1181.7
F606W	POL120V	2016 Apr 08	4 × 311	796.8	2016 Oct 14	3 × 360	985.1	2017 Apr 28	3 × 360	1181.7
F606W	POL60V	2016 Apr 08	4 × 311	796.9	2016 Oct 14	3 × 360	985.1	2017 Apr 28	3 × 360	1181.7
F775W	POL0V	2016 Apr 08	4 × 100	796.2	2016 Oct 12	4 × 202	983.1	2017 Apr 28	4 × 202	1181.3
F775W	POL120V	2016 Apr 08	4 × 100	796.4	2016 Oct 12	4 × 202	983.3	2017 Apr 28	4 × 202	1181.4
F775W	POL60V	2016 Apr 08	4 × 100	796.6	2016 Oct 12	4 × 202	983.4	2017 Apr 28	4 × 202	1181.5

Note.
[a] Days since B maximum on 2014 February 2.0 (JD 245 6690.5).

Goobar et al. 2014; Brown et al. 2015; Gao et al. 2015). In this study, we adopt $R_V = 1.44 \pm 0.03$ and $A_V = 2.07 \pm 0.18$ mag from Foley et al. (2014) for the extinction from the host galaxy and $R_V = 3.1$ and $E(B-V) = 0.054$ mag for the Galactic extinction following Foley et al. (2014) based on Dalcanton et al. (2009) and Schlafly & Finkbeiner (2011). Extinction in the *F475W*, *F606W*, and *F775W* bands has been calculated for each component using a reddening law from Cardelli et al. (1989) with the corresponding R_V value. Both components are added to account for the total extinction toward SN 2014J for each *HST* ACS bandpass.

3. Analysis

In this section, we will test different mechanisms powering the late-time light curve, and whether the light curve behavior is consistent with the prediction for the delayed-detonation and the violent merger scenarios following a similar procedure to Graur et al. (2016) for SN 2012cg. We assume that the ejecta do not interact with any circumstellar material.

3.1. Pseudo-bolometric Light Curve

The pseudo-bolometric light curve for SN 2014J was calculated over a wavelength range from 3500 to 9000 Å based on our multi-band optical photometry. We briefly summarize the steps as follows:

(1) Based on the lack of significant spectral evolution of SN 2011fe compared to a spectrum at 593 days (Graham et al. 2015), we assume the MODS/LBT spectrum of SN 2011fe at 1016 days (Taubenberger et al. 2015) represents the major spectral features of SN 2014J on V3 ∼ day 649, V4 ∼ day 796, V5 ∼ day 983, and V6 ∼ day 1181. The spectrum was retrieved from the WISeREP archive.[13]
(2) We then perform synthetic photometry on this spectrum for the *F475W*, *F606W*, and *F775W* bands.
(3) We calculate the differences between the synthetic photometry of the SN 2011fe spectrum and our extinction-corrected, observed photometry of SN 2014J.
(4) We calculate the scale factors between the observed and synthetic magnitudes in each filter.
(5a) We warp the spectrum using a second-order polynomial fit to the scale factors determined at the effective wavelength for each filter.[14]
(5b) Alternatively, for each epoch, we fit a single wavelength-independent grayscale across all wavelengths.
(6) We iterate steps (2)–(5) until the synthetic and observed photometry match to better than 0.02 mag in each filter for (5a), or the mean difference between the synthetic and the observed photometry converges to its minimum value for (5b), for which the standard deviation among the three filters is 0.11 mag.

The pseudo-bolometric luminosity for each epoch was obtained by integrating the scaled spectrum returned from (5a) or (5b) over the wavelength range 3500–9000 Å. The errors on the pseudo-bolometric light curve were computed through a Monte Carlo re-sampling approach using the photometric errors. The warping in (5a) aims at iteratively producing spectra consistent with the photometry, which follows a procedure very similar to that described in Shappee et al. (2016), while the scaling in (5b) is less sensitive to the extrapolation of the polynomial correction to the spectrum. The pseudo-bolometric luminosities calculated from (5a) are on average 13% higher than those from (5b). This discrepancy results from the construction of pseudo-bolometric light curves. For the scientific consideration of our study, this systematic difference does not affect the measurement of the abundance ratio affecting the decline rate of the SN luminosity. After

[13] http://wiserep.weizmann.ac.il

[14] http://pysynphot.readthedocs.io/en/latest/properties.html#pysynphot-formula-efflam

Table 2
HST ACS/WFC Late-time Photometry of SN 2014J

Filter	*F475W*		*F606W*		*F775W*		log L^b
Visit	Phase[a]	AB Magnitude	Phase[a]	AB Magnitude	Phase[a]	AB Magnitude	(erg s^{-1})
1	276.5	17.363 ± 0.003	276.6	17.429 ± 0.003	276.6	16.742 ± 0.004	40.279 ± 0.017
2	415.6	19.464 ± 0.003	418.0	19.602 ± 0.004	418.0	18.276 ± 0.005	39.482 ± 0.018
3	648.7	22.363 ± 0.004	649.0	21.962 ± 0.005	648.7	21.427 ± 0.007	38.346 ± 0.030
4	796.4	23.266 ± 0.007	796.8	22.917 ± 0.013	796.4	22.492 ± 0.012	37.968 ± 0.023
5	983.3	24.169 ± 0.016	985.1	23.936 ± 0.032	983.3	23.294 ± 0.016	37.592 ± 0.019
6	1181.4	24.765 ± 0.026	1181.7	24.695 ± 0.060	1181.4	24.234 ± 0.057	37.308 ± 0.039

Notes.
[a] Approximate days after *B* maximum, 2014 February 2.0 (JD 245 6690.5).
[b] Phases in *F475W* have been used.

correcting this discrepancy, the pseudo-bolometric luminosities calculated from these two approaches agree within 8% at all epochs, compatible with the uncertainties of the Monte Carlo approach. The error used in fitting the ratio of the isotopes has been estimated by adding this difference to the uncertainties obtained from the Monte Carlo approach in quadrature. The pseudo-bolometric luminosity of SN 2014J is listed in Table 2. The optical pseudo-bolometric luminosity at $t \sim 277$ days after the *B*-band maximum ($\log L \approx 40.28$) is roughly consistent with the UVOIR bolometric luminosity at $t \sim 269$ days ($\log L \approx 40.35$) estimated from Figure 8 of Srivastav et al. (2016). Our analysis of the bolometric evolution of SN 2014J is based on the bolometric luminosity obtained with (5b). Qualitatively similar results have been obtained by duplicating the entire analysis based on (5a) as follows.

In Figure 2 we present the spectra constructed using the warping procedure (left panel) and with grayscaling (right panel). For comparison, in each upper panel, we overplot the bandpass monochromatic flux calculated as the product Total Counts × PHOTFLAM,[15] where PHOTFLAM is the inverse sensitivity (in erg cm^{-2} s^{-1} Å^{-1}) representing a signal of 1 electron per second. The lower panels present the total bandpass throughput curve (*HST* + ACS)[16] for our *F475W*, *F606W*, and *F775W* observations. The spectra on the left panel are iterated to agree quantitatively with the photometry. Visual differences between the monochromatic bandpass flux and the spectra arise because the PHOTFLAM used for the SED assumes a smooth AB spectrum, which differs from the SN spectrum (see Brown et al. 2016 for a comprehensive discussion).

3.2. Radioactive Decay

In the left panels of Figure 3, we present the *F475W*, *F606W*, and *F775W*-band luminosities of SN 2014J after correction for extinction. In addition to fitting the pseudo-bolometric light curve after ~650 days with the contribution from three decay chains: ^{56}Co → ^{56}Fe, ^{57}Co → ^{57}Fe, and ^{55}Fe → ^{55}Mn (an "all isotopes" model), we also fit the same model to our *F606W*-band observations. Here, we have assumed that after ~500 days the *F606W*-band, which is centered at wavelength 5888.8 Å and with a width[17] of 2570 Å, captures the dominant Fe features ([Fe II] around 4700 and 5300 Å, blended [Fe II] λ7155 and [Ni II]λ7378 around 7200 Å; Taubenberger et al. 2015), and is proportional to the bolometric light curves as *V*-band observations (Milne et al. 2001).

Limited by a small number of visits, we approximate the "all isotopes" model with two free parameters: the mass ratio $M(^{57}\mathrm{Co})/M(^{56}\mathrm{Co})$, and a scale factor to match the *F606W* photometry (or the pseudo-bolometric luminosity) with the model-calculated values. Using the solution to the Bateman equation that describes the abundances and activities in a decay chain as a function of time (following Seitenzahl et al. 2014), and by counting the decay energy carried by charged leptons and X-rays, the luminosity contribution from a single decay chain gives:

$$L_A(t) = 2.221 \frac{C}{A} \frac{\lambda_A}{\mathrm{day\ s^{-1}}} \frac{M(A)}{M_\odot} \frac{q_A^l + q_A^X}{\mathrm{keV}} \exp(-\lambda_A t_e) \times 10^{43}\ \mathrm{erg\ s^{-1}}, \quad (2)$$

where *C* is a scaling factor, *A* gives the corresponding atomic number, λ_A is the inverse mean lifetime ($\lambda_A = \tau_A^{-1} = \ln(2)/t_{1/2,A}$), $M(A)$ is the total mass of a certain decaying element, q_A^l and q_A^X are the average energies per decay carried by charged leptons and X-rays, respectively, and t_e is the time since explosion. Due to the limited data points in our late-time photometry, we used a ratio of $M(^{57}\mathrm{Co})/M(^{55}\mathrm{Fe}) \approx 0.8$ (model rpc32; Ohlmann et al. 2014). The values of λ_A, q_A^l and q_A^X used here are sourced from Table 1 of Seitenzahl et al. (2009) and Table 2 of Seitenzahl et al. (2014). We justify our assumptions as follows. (1) The total deposition function is determined by both the net deposition functions for γ-rays and positrons. The γ-rays produced by the annihilation of the positrons are subject to both deposition functions. By simply assuming the radioactive source is confined to the center of a spherical distribution of ejecta yields a fraction $1 - e^{-\tau_\gamma}$ of the energy produced by γ-rays would be left behind in the ejecta (Swartz & Wheeler 1991). The γ–ray optical depth τ_γ drops significantly as t^{-2} and we neglect contributions from γ-rays because the SN ejecta became transparent to γ-rays at $t \gtrsim 500$ days (Milne et al. 2001). (2) Limited by a small number of photometric points, we begin by fitting Equation (2) assuming full trapping of positrons/electrons. In other words, we assume positrons, electrons, and X-rays are fully trapped, instantaneously deposited, and radiate their energy. One should also note that very recently, Dimitriadis et al. (2017) found that the late-time bolometric light curve of SN 2011fe is consistent with both

[15] This can be obtained with the ACS Zeropoints Calculator at https://acszeropoints.stsci.edu/.
[16] http://www.stsci.edu/hst/acs/analysis/throughputs
[17] Where the filter throughput is larger than 0.05%.

Table 3
HST Late-time Light Curve Decline Rate of SN 2014J

Period[a]\Filter (Days)	*F475W* (Δmag/100 days)	*F606W* (Δmag/100 days)	*F775W* (Δmag/100 days)	Pseudo-bolometric (Δmag/100 days)
277–416	1.511 ± 0.003	1.532 ± 0.004	1.079 ± 0.004	1.432 ± 0.044
416–649	1.245 ± 0.002	1.024 ± 0.003	1.370 ± 0.003	1.219 ± 0.038
649–796	0.611 ± 0.006	0.646 ± 0.009	0.721 ± 0.009	0.640 ± 0.064
796–983	0.483 ± 0.009	0.540 ± 0.018	0.429 ± 0.011	0.503 ± 0.040
983–1181	0.301 ± 0.015	0.387 ± 0.035	0.474 ± 0.030	0.358 ± 0.055

Note.
[a] Approximate days after *B* maximum, 2014 February 2.0 (JD 245 6690.5).

models: either a model that allows for positron/electron escape, or a model that has complete positron/electron trapping but allows for redistribution of flux to the mid-far-IR.

The luminosity contribution from each decay channel is shown in Figure 3. The total luminosity given by these decay chains is represented by the pink dashed line. In the left panel, we show that a mass ratio of $M(^{57}\mathrm{Co})/M(^{56}\mathrm{Co}) = 0.065^{+0.005}_{-0.004}$ gives the best fit to the "all isotopes" model based on the *F606W*-band observations after $t \sim 500$ days (V3–V6). The dot-dashed gray lines show the model including the luminosity from ^{56}Co decay and possible reflections from an unresolved t^{-1} light echo (see Graur et al. 2016). In the right panel, we show the same trend in a similar fitting based on the pseudo-bolometric light curve, with the mass ratio given as $M(^{57}\mathrm{Co})/M(^{56}\mathrm{Co}) = 0.066^{+0.009}_{-0.008}$. We also tested the same abundance ratio, using a fit based on the pseudo-bolometric light curve constructed with the warped spectrum (procedure 5a in Section 3). A similar mass ratio of $M(^{57}\mathrm{Co})/M(^{56}\mathrm{Co}) = 0.078^{+0.011}_{-0.010}$ was obtained.

3.3. Light Echoes?

If light echoes dominate the late time signal from the SN, we may expect a significant profile change or centroid drift if the circumstellar matter is distributed at sufficiently large distances from the SN. Light scattered by dust at such distances can produce measurable distortions to the image profiles if the scattered light dominates the total observed flux. At the distance of SN 2014J, 1 lt-yr corresponds to 0.17 *HST* ACS/WFC pixels. Depending on the dust distribution, we may expect the stellar profiles to become non-point-like, or the centroid of the stellar profile to drift at late times. We have checked the stellar profiles and found no significant deviations from a point source at all epochs of our observations. In the following, we provide a comprehensive check on the centroid position of the SN.

The barycenters of the stars and H II regions around SN 2014J were measured to estimate a possible change in the relative position of the light emission of the SN. The precision is limited by the scarcity of stars in the immediate vicinity of the SN, as well as the uncharacterized field distortions caused by ACS/WFC polarizers (see, i.e., Section 5.3 of Gonzaga et al. 2012). Figure 4 presents the apparent shift in position measured from our observations in *F475W* and *F606W*. The R.A. and decl. were calculated using the image from V3, with the SN at the origin of the coordinates. The gray arrows show the vector difference of the originally measured positions of the source on two different epochs. The black arrow shows the same vector after a 2D linear regression to remove the dependence on R.A. and decl., which may be caused by residual errors of astrometric calibrations. The linear regression was found to be able to reduce the shift significantly in all cases. The reference objects for astrometric comparisons were selected within a radius of 500 pixels of the position of the SN. The FWHM of the objects was restricted to be less than 8 pixels. Only a small number objects in the earliest epoch V1 satisfy these criteria, due to the relatively short exposure time.

In Figure 4, the upper panels present the measurements based on the highest S/N *F475W*-band exposures, and the lower panels present the same figures for *F606W*. For V5 and V6, when the the SN became sufficiently dim, to minimize the effect of the local background, the centroid of the SN was determined based on scaled and background subtracted images. For instance, in the upper row, the first panel presents the comparison between V3 and V1. The SN (red dot) exhibits an apparent motion of 0.″079 (gray arrow); after linear regression with the R.A. and decl., this reduces to 0.″029 (black arrow). This is in agreement with all the other objects in the field, which show an average distance shift of 0.″022 and an rms of 0.″014. The second panel presents the comparison between V3 and V2. The SN exhibits an apparent drift in position of 0.″020; after linear regression this reduces to 0.016. The field objects exhibit an average drift of 0.″036 and an rms of 0.″023. This implies that the position drift of the SN is significantly lower than the average of the field objects. The third to the fifth panels present the comparison between V3 and V4, V3 and V5, V3 and V6, respectively. After linear regression with R.A. and decl., using the stars around the SN, the drift of the SN compared to the average drift ±rms gives: 0.″015 versus 0.024 ± 0.″016, 0.″008 versus 0.021 ± 0.″016, and 0.″031 versus 0.027 ± 0.″017, respectively. An upper bound on the centroid position drift of the SN between V3 and another epoch is thus observed to be the sum of the SN drift and the rms of the drift measured from field objects. In each of these cases, this upper bound has been found to be larger than the average drift of the field objects, which implies that there is no apparent position drift of the SN. Similar results were obtained for *F606W*-band exposures. In all cases, we have not observed a significant position drift of the SN. The only exception is the 0.″077 versus 0.″031 ± 0.″018 in V3 compared to V6, *F606W*. Considering no drift was found in the same epoch of *F475W* and the low signal-to-noise ratio of the *F606W* observation, we do not consider significant drift of the SN in V6. The absence of such drift sets a strong constraint on the nature of the late-time emission from SN 2014J. If the significant flattening in *F606W*-band and pseudo-bolometric light curves is due to light echoes, the dust must lie within 0.″017 of the SN.

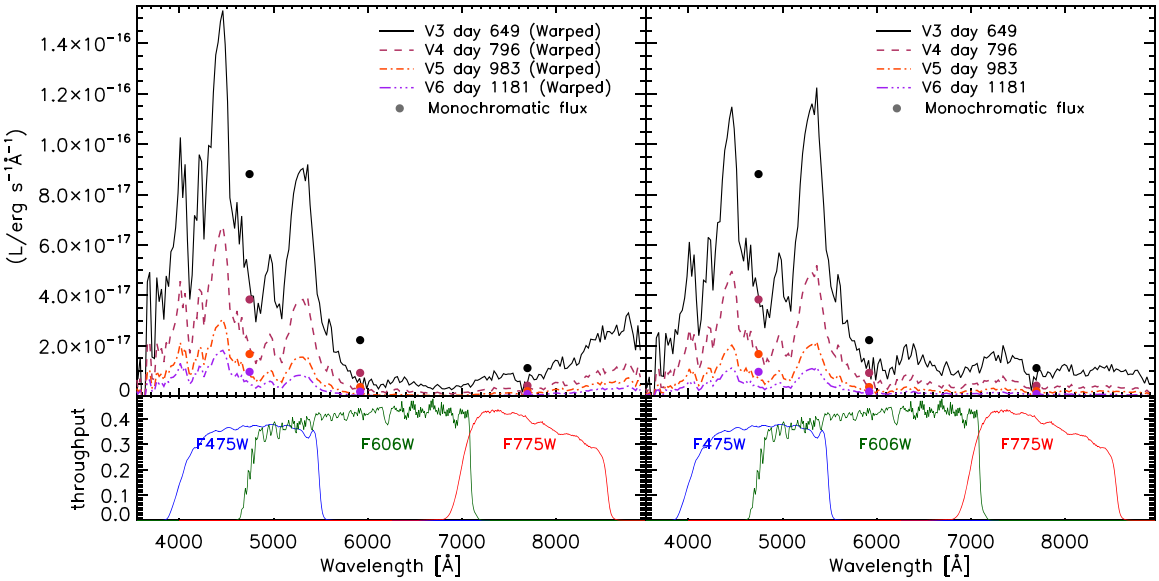

Figure 2. Constructed late-time SED for SN 2014J. The dots show the bandpass monochromatic flux from *HST* observations at their effective wavelengths. The solid, dashed, dashed–dotted, and triple-dotted–dashed lines show the spectra constructed with the warping procedure (left panel) and with grayscaling (right panel) as described in Section 3, from V3 to V6, respectively. The lower panels present the total bandpass throughput curve (*HST* + ACS) for our *F*475*W*, *F*606*W*, and *F*775*W* observations, showing the spectral response corresponding to the monochromatic fluxes calculated from the observed photometry.

Here, we address the possibility of an unresolved light echo within the PSF of the late-time source at the SN position. Our photometry allows us to measure the *F*475*W*–*F*606*W* and *F*606*W*–*F*775*W* colors at very late phases. We also compared the late-time color evolution of SN 2014J with SN 2011fe, which does not exhibit evident flux contribution from the light echoes. Light-echo flux is dominated by the light of the SN around its peak, and scattering by dust favors blue light. At extremely late phases, when light from the SN may no longer dominate over the scattered light echoes, the color of the integrated flux can appear to be bluer by a few tenths of a magnitude (Rest et al. 2012; Graur et al. 2016). A redder color measured at a very late time, therefore, would suggest the absence of a light echo. In Figure 5, we present a comparison of the late-time color evolution of SN 2014J and SN 2011fe. The *B*- and *V*-band AB magnitudes of SN 2014J were calculated with PYSYNPHOT using the grayscaled spectrum introduced in (5b) in Section 3. Systematic differences between the synthetic photometry in *F*475*W* and *F*606*W* on the grayscaled and the *HST* photometry were included when calculating the error in the $B - V$ color of SN 2014J.

The $B - V$ color of SN 2014J from $t \sim -8$ to 269 days has been calculated based on the photometry of Srivastav et al. (2016). The $B - V$ color curves of SN 2011fe at early (Zhang et al. 2016) and at late (Shappee et al. 2016) phases are shown for comparison. We note that from days ∼140 to 500, the $B - V$ color of SN 2014J appears to be bluer than it was around the maximum light (see, i.e., Figure 5). A similar effect can be expected if SN 2014J was contaminated by light echoes. The color of SN 2014J at days ∼650 to 1200 is redder, however, in $B - V$ by ∼0.3 mag, and the color evolution of SN 2014J also shows a similar trend to that of SN 2011fe at the same phase. Spectra of SN 2011fe at day ∼1000 detected no trace of a light echo (Graham et al. 2015; Taubenberger et al. 2015). Thus, the similarity in the late-time color evolutions of SN 2014J and SN 2011fe, together with our astrometric analysis, lead us to argue that the luminosity measurement of SN 2014J was not contaminated by a light echo at days ∼650 to 1200.

4. Discussion and Summary

Table 3 shows the decline rate of the light curves at different epochs. Before $t \sim 600$ days, the SN dims more rapidly than the light curve powered solely by the ^{56}Co decay. The γ-ray energy deposition becomes no longer significant after ∼200 days, therefore a substantial fraction of the flux may be shifting out of the optical bands into the infrared. Similar behavior has been discussed in the case of SN 2011fe (Kerzendorf et al. 2014) and SN 2003hv (Leloudas et al. 2009). After $t \sim 600$ days, a slower decay can be identified in all the *F*475*W*, *F*606*W*, and *F*775*W*-bandpasses.

Some observations of nearby type Ia SNe show that their bolometric light curves at late phases follow the ^{56}Co decay channel (Cappellaro et al. 1997; Sollerman et al. 2004; Lair et al. 2006; Stritzinger & Sollerman 2007; Leloudas et al. 2009). These observations suggest that a turbulent, confining magnetic field traps the positrons, resulting in local energy deposition (see Chan & Lingenfelter 1993; Milne et al. 1999, 2001; Penney & Hoeflich 2014). In contrast, ^{56}Co positron escape has been suggested in some cases (Milne et al. 1999, 2001). As the ejecta expand over time, the pre-configured magnetic field weakens to the point that the Larmor radius exceeds the size of the turbulence (see Penney & Hoeflich 2014).

The late-time pseudo-bolometric decline rate of SN 2014J during day 277 to day 416 (1.432 ± 0.044 mag per 100 days) and day 416 to day 649 (1.219 ± 0.038) is larger than the predicted decay rate of radioactive ^{56}Co (0.98 mag per 100 days). This may be caused by the positron escape, which would produce a faster decay rate. A similar decline rate can also be seen in the quasi-bolometric light curve of SN 2014J at ∼days 238–269 (i.e., ∼1.3 mag per 100 days; Srivastav et al. 2016). Qualitatively speaking, at these intermediate epochs, the contributions from γ-rays may still be non-negligible since

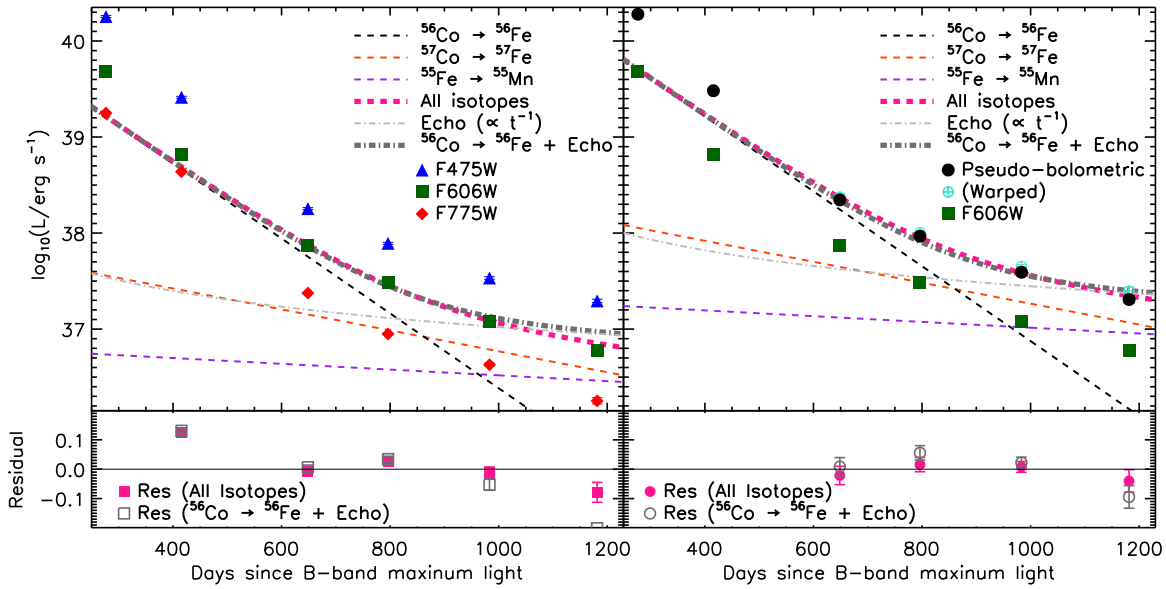

Figure 3. Luminosity evolution of the monochromatic fluxes from the broadband observations (left panel) and pseudo-bolometric flux (right panel) with possible mechanisms explaining the flattening of the light curves of SN 2014J. The left panel presents the fitting and residuals of V3–V6 based on *F606W*-band observations, while the right panel shows a similar plot based on the constructed pseudo-bolometric luminosity. In the left panel, we also present the *F475W* and *F775W*-band observations. The *F606W*-band observations, together with the pseudo-bolometric light curve constructed with a warped spectrum (procedure 5a in Section 3, cyan ⊕), are shown in the right panel for comparison. The *F606W*-band observations after ∼650 days have been assumed to be proportional to the bolometric light curves (Milne et al. 2001) and free from possible γ-ray photons. Only observations after 650 days have been fitted with models accounting for all the listed isotopes or ^{56}Co plus a faint, unresolved light echo.

the SN ejecta may not have become transparent to γ-ray photons.

We fit both the *F606W*-band and a "pseudo-bolometric" light curve using Bateman's equation for the luminosity contribution of the ^{56}Co, ^{57}Co, and ^{55}Fe decay channels. The best fit to the pseudo-bolometric light curve and the *F606W*-band light curve give mass ratios of $M(^{57}\mathrm{Co})/M(^{56}\mathrm{Co}) = 0.065^{+0.005}_{-0.004}$ and $0.066^{+0.009}_{-0.008}$, respectively. Assuming the same mass ratio yields for isotopes of the same iron-group elements (see Graur et al. 2016, based on Truran et al. 1967 and Woosley et al. 1973), our measurements correspond to ∼3 times the $M(^{57}\mathrm{Fe})/M(^{56}\mathrm{Fe})$ ratio of the Sun (i.e., ∼0.0217, see Table 3 of Asplund et al. 2009). This is higher than the solar ratio of ∼1.8 predicted for the W7 model (calculated from Table 3 of Iwamoto et al. 1999), and the solar ratio of ∼1.7 predicted for the near-Chandrasekhar-mass 3D delayed-detonation model N1600 (calculated from Table 2 of Seitenzahl et al. 2013). The $M(^{57}\mathrm{Fe})/M(^{56}\mathrm{Fe})$ ratio in our measurements is also higher compared to the ratios of ∼2 and ∼1.1 suggested by the late-time quasi-bolometric light curve analysis on SN 2012cg (Graur et al. 2016) and SN 2011fe (Shappee et al. 2016). A higher-metallicity progenitor could decrease the production of ^{56}Ni and result in a higher $M(^{57}\mathrm{Ni})/M(^{56}\mathrm{Ni})$ ratio (Seitenzahl et al. 2013). An enhancement of neutron excess due to electron captures in the deflagration wave could lead to the same effect.

It has been suggested that beyond ∼500 days in the ejecta, energy is shifted from the optical and near-infrared to the mid- and far-infrared (referred to as the infrared catastrophe; Axelrod 1980, and see Fransson et al. 1996; Fransson & Jerkstrand 2015). The *V* or optical luminosity may not represent the actual behavior of the bolometric light curves. This has never been observed so far in any type Ia SNe (e.g., Sollerman et al. 2004; Leloudas et al. 2009; Kerzendorf et al. 2014; McCully et al. 2014; Graur et al. 2016; Shappee et al. 2016). However, Dimitriadis et al. (2017) suggested that the evolution of SN 2011fe, around 550 to 650 days, is consistent with both a model that allows for positron/electron escape and a model allowing for a redistribution of flux from the optical to the mid-far-infrared. In our study, we fitted the *F606W*-band and optical bolometric luminosity after ∼650 days and did not consider the infrared catastrophe. Future studies based on a larger sample will be able to help distinguish these two possible scenarios.

As suggested by Kerzendorf et al. (2017), although the flattening of the late-time light curves of SN 2014J can be explained by additional energy input from the decay of ^{57}Co, we concede that one cannot draw strong conclusions from the current observation due to the uncertain physical processes. The determination of a precise isotopic abundance requires detailed modeling of the processes. Another mechanism that may plausibly explain the late-time luminosity-flattening is the survival of the donor WD after the explosion. A small amount of ^{56}Ni-rich material synthesized by the primary WD's explosion at low velocities might remain gravitationally bound and captured by the surviving WD companion (Shen & Schwab 2017). The lack of electrons on the surface of the donor WD significantly reduces the decay rates of ^{56}Ni and ^{56}Co more than electron capture (Sur et al. 1990; da Cruz et al. 1992). The radioactive decay is delayed, thus the surviving WD can be another source of late-time type Ia SN luminosity. Future observations of type Ia SNe at extremely late phases will be important for understanding the physical processes at this late stage and further testing the explosion mechanisms of type Ia SNe.

In summary, our multi-band photometry of SN 2014J out to 1181 days past the *B*-band maximum light clearly detected the flattening due to extra luminosity contributions other than the decay of ^{56}Co. We conclude that the high $M(^{57}\mathrm{Ni})/M(^{56}\mathrm{Ni})$ ratio estimated from the late-time luminosity evolution of

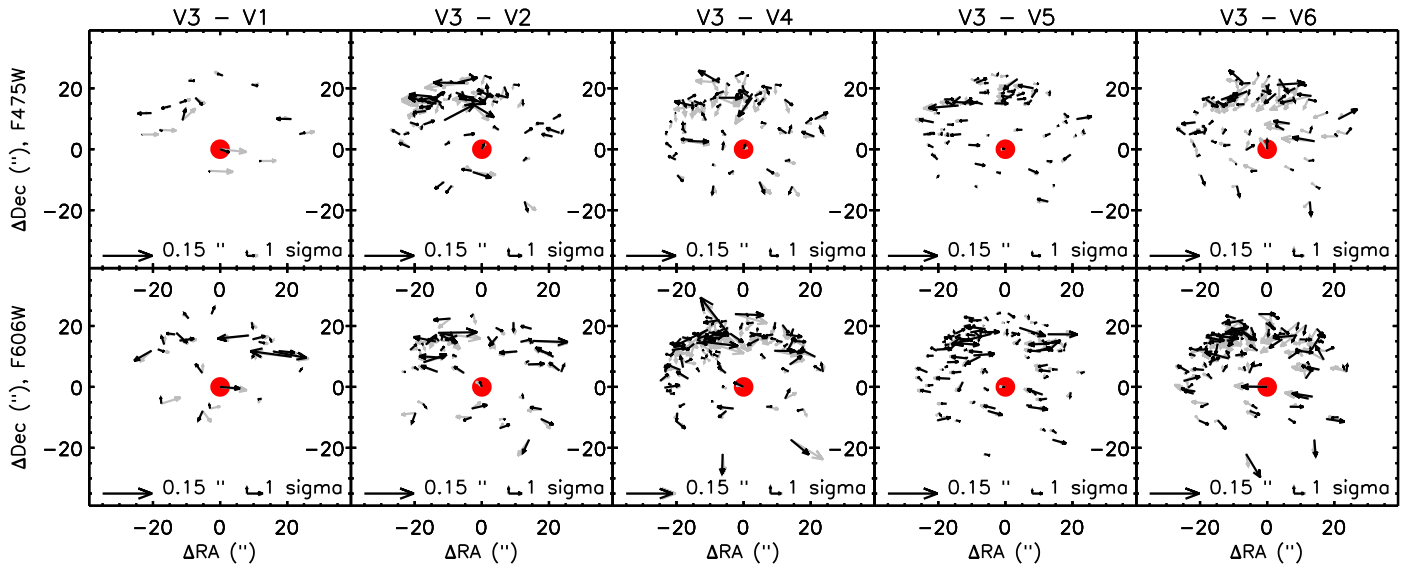

Figure 4. Astrometric comparisons of different visits. The x and y axes are the positions of bright sources relative to SN 2014J, most of which are H II regions in M82. The SN is represented by the red dot at the origin. The gray and black arrows are the relative motions between different visits prior to and after a linear regression with the R.A. and decl. 1σ displacements calculated based on all the presented sources and scales are provided at the bottom right of each panel. No significant positional drift of the SN is found among all the cases, suggesting the absence of any circumstellar light echoes around 1 lt-yr from the SN on the plane of the sky.

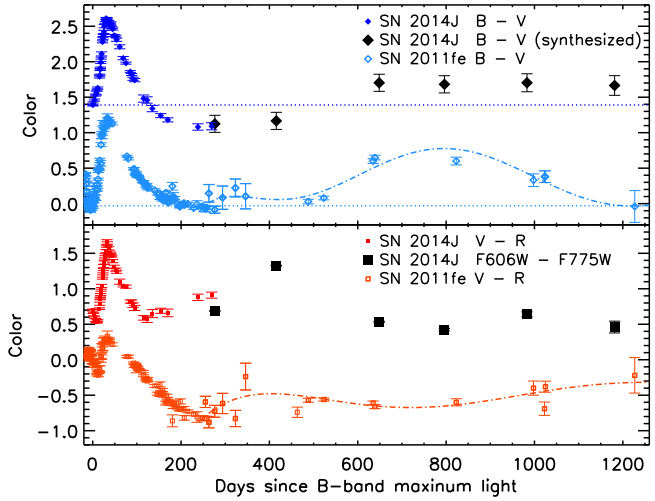

Figure 5. Comparison of the color evolution of SN 2014J and SN 2011fe until very late phases to address the possibility of an unresolved light echo within the PSF. The top panel presents the $B-V$ color calculated with PYSYNPHOT based on the grayscaled spectrum of SN 2014J at late epochs and the $B-V$ color of SN 2014J from $t\sim -8$ to 269 days (Srivastav et al. 2016). The $B-V$ color curves of SN 2011fe at early (Zhang et al. 2016) and at late (Shappee et al. 2016) epochs are shown for comparison. The dotted–dashed lines show polynomial fits to the color evolution after day ~250 and the horizontal dashed lines indicate the color at the SN maximum. The fact that SN 2014J has become redder than it was at both its peak and SN 2011fe at similar epochs, limits the flux any light echo could be contributing. The bottom panel gives the evolution of the $F606W-F775W$ color of SN 2014J and the $V-R$ color of SN 2011fe for comparison.

SN 2014J favors a near-Chandrasekhar-mass explosion model such as W7 of Iwamoto et al. (1999). Any significant circumstellar light echoes beyond 0.3 pc on the plane of the sky can be excluded by our astrometric analysis. The observations strongly suggest additional heating from internal conversion and Auger electrons of $^{57}\mathrm{Co}\rightarrow{}^{57}\mathrm{Fe}$; however, one should be cautious on the high mass ratio of $^{57}\mathrm{Ni}$ to $^{56}\mathrm{Ni}$. Systematic uncertainties from the SED construction procedure, especially the missing information from NIR observations and the interpolation of the SED based on limited bandpass coverage should not be ignored (i.e., see Brown et al. 2016). Additionally, the reliability of approximating the bolometric luminosity evolution after $t\sim 650$ days with the $F606W$-band emission requires more careful justification.

The authors are grateful to Dave Borncamp and the *HST* ACS team for fixing the distortion correction issues in the ACS/WFC polarized images. We would like to thank the anonymous referee and Or Graur for the very helpful discussions and constructive suggestions that improved the paper. Some of the data used in this study were obtained from the Mikulski Archive for Space Telescopes (MAST). STScI is operated by the Association of Universities for Research in Astronomy, Inc., under NASA contract NAS5-26555. Support for MAST for non-*HST* data is provided by the NASA Office of Space Science via grant NNX09AF08G and by other grants and contracts. This work also made use of the Weizmann interactive supernova data repository (WISeREP). The supernova research by Y. Yang, P. J. Brown, and L. Wang is supported by NSF grant AST-0708873. P. J. Brown was partially supported by a Mitchell Postdoctoral Fellowship. Y. Yang and M. Cracraft also acknowledge support from NASA/STScI through grant *HST*-GO-13717.001-A, grant *HST*-GO-13717.001-A, *HST*-GO-14139.001-A, and *HST*-GO-14663.001-A. The research of Y. Yang is supported through a Benoziyo Prize Postdoctoral Fellowship. The research of J. Maund is supported through a Royal Society University Research Fellowship. L. Wang is supported by the Strategic Priority Research Program "The Emergence of Cosmological Structures" of the Chinese Academy of Sciences, Grant No. XDB09000000. L. Wang and X. Wang are supported by the Major State Basic Research Development Program (2013CB834903), and X. Wang is also supported by the National Natural Science Foundation of China (NSFC grants 11178003 and 11325313).

ORCID iDs

Yi Yang https://orcid.org/0000-0002-6535-8500
Peter. J. Brown https://orcid.org/0000-0001-6272-5507
Misty Cracraft https://orcid.org/0000-0002-7698-3002
Justyn R. Maund https://orcid.org/0000-0003-0733-7215
Ferdinando Patat https://orcid.org/0000-0002-0537-3573
William B. Sparks https://orcid.org/0000-0002-9011-6829
Jason Spyromilio https://orcid.org/0000-0001-6815-4055
Heloise F. Stevance https://orcid.org/0000-0002-0504-4323
Xiaofeng Wang https://orcid.org/0000-0002-7334-2357
J. Craig Wheeler https://orcid.org/0000-0003-1349-6538

References

Amanullah, R., Goobar, A., Johansson, J., et al. 2014, ApJL, 788, L21
Arnett, W. D. 1979, ApJL, 230, L37
Arnett, W. D. 1982, ApJ, 253, 785
Asplund, M., Grevesse, N., Sauval, A. J., & Scott, P. 2009, ARA&A, 47, 481
Axelrod, T. S. 1980, PhD thesis, California Univ.
Biretta, J., Kozhurina-Platais, V., Boffi, F., Sparks, W., & Walsh, J. 2004, ACS Polarization Calibration—I. Introduction and Status Report, Instrument Science Report, ACS 2004-09
Bonanos, A. Z., & Boumis, P. 2016, A&A, 585, A19
Brown, P. J., Breeveld, A., Roming, P. W. A., & Siegel, M. 2016, AJ, 152, 102
Brown, P. J., Smitka, M. T., Wang, L., et al. 2015, ApJ, 805, 74
Cappellaro, E., Mazzali, P. A., Benetti, S., et al. 1997, A&A, 328, 203
Cardelli, J. A., Clayton, G. C., & Mathis, J. S. 1989, ApJ, 345, 245
Chan, K.-W., & Lingenfelter, R. E. 1993, ApJ, 405, 614
Churazov, E., Sunyaev, R., Isern, J., et al. 2014, Natur, 512, 406
Cracraft, M., & Sparks, W. B. 2007, ACS Polarization Calibration—Data, Throughput, and Multidrizzle Weighting Schemes, Instrument Science Report, ACS 2007-10
da Cruz, M. T., Chan, Y., Larimer, R.-M., et al. 1992, PhRvC, 46, 1132
Dalcanton, J. J., Williams, B. F., Seth, A. C., et al. 2009, ApJS, 183, 67
Denisenko, D., Gorbovskoy, E., Lipunov, V., et al. 2014, ATel, 5795, 1
Diehl, R., Siegert, T., Hillebrandt, W., et al. 2015, A&A, 574, A72
Dimitriadis, G., Sullivan, M., Kerzendorf, W., et al. 2017, arXiv:1701.07267
Foley, R. J., Fox, O. D., McCully, C., et al. 2014, MNRAS, 443, 2887
Fossey, J., Cooke, B., Pollack, G., Wilde, M., & Wright, T. 2014, CBET, 3792, 1
Fransson, C., Houck, J., & Kozma, C. 1996, in IAU Coll. 145: Supernovae and Supernova Remnants, ed. R. McCray & Z. Wang (Cambridge: Cambridge Univ. Press), 211
Fransson, C., & Jerkstrand, A. 2015, ApJL, 814, L2
Gao, J., Jiang, B. W., Li, A., Li, J., & Wang, X. 2015, ApJL, 807, L26
Gerke, J. R., Kochanek, C. S., & Stanek, K. Z. 2014, ATel, 5808, 1
Gonzaga, S., Hack, W., Fruchter, A., & Mack, J. 2012, The DrizzlePac Handbook (Baltimore: STScI)
Goobar, A., Johansson, J., Amanullah, R., et al. 2014, ApJL, 784, L12
Graham, M. L., Nugent, P. E., Sullivan, M., et al. 2015, MNRAS, 454, 1948
Graur, O., Zurek, D., Shara, M. M., et al. 2016, ApJ, 819, 31
Graur, O., Zurek, D. R., Rest, A., et al. 2017, arXiv:1711.01275
Hartig, G. F. 2009, WFC3 SMOV Programs 11436/8, UVIS On-orbit PSF Evaluation, Instrument Science Report, WFC3 2009-38
Hoyle, F., & Fowler, W. A. 1960, ApJ, 132, 565
Itagaki, K., Kaneda, H., Yamaoka, H., et al. 2014, CBET, 3792, 2
Iwamoto, K., Brachwitz, F., Nomoto, K., et al. 1999, ApJS, 125, 439
Johansson, J., Goobar, A., Kasliwal, M. M., et al. 2017, MNRAS, 466, 3442
Kerzendorf, W. E., McCully, C., Taubenberger, S., et al. 2017, MNRAS, 472, 2534
Kerzendorf, W. E., Taubenberger, S., Seitenzahl, I. R., & Ruiter, A. J. 2014, ApJL, 796, L26
Khokhlov, A. M. 1991, A&A, 245, 114
Lair, J. C., Leising, M. D., Milne, P. A., & Williams, G. G. 2006, AJ, 132, 2024
Leloudas, G., Stritzinger, M. D., Sollerman, J., et al. 2009, A&A, 505, 265
Lundqvist, P., Nyholm, A., Taddia, F., et al. 2015, A&A, 577, A39
Ma, B., Wei, P., Shang, Z., Wang, L., & Wang, X. 2014, ATel, 5794, 1
McCully, C., Jha, S. W., Foley, R. J., et al. 2014, ApJ, 786, 134
Milne, P. A., The, L.-S., & Leising, M. D. 1999, ApJS, 124, 503
Milne, P. A., The, L.-S., & Leising, M. D. 2001, ApJ, 559, 1019
Ohlmann, S. T., Kromer, M., Fink, M., et al. 2014, A&A, 572, A57
Pakmor, R., Hachinger, S., Röpke, F. K., & Hillebrandt, W. 2011, A&A, 528, A117
Pakmor, R., Kromer, M., Taubenberger, S., et al. 2012, ApJL, 747, L10
Penney, R., & Hoeflich, P. 2014, ApJ, 795, 84
Perlmutter, S., Aldering, G., Goldhaber, G., et al. 1999, ApJ, 517, 565
Rest, A., Sinnott, B., & Welch, D. L. 2012, PASA, 29, 466
Riess, A. G., Filippenko, A. V., Challis, P., et al. 1998, AJ, 116, 1009
Riess, A. G., Macri, L. M., Hoffmann, S. L., et al. 2016, ApJ, 826, 56
Röpke, F. K., Kromer, M., Seitenzahl, I. R., et al. 2012, ApJL, 750, L19
Schlafly, E. F., & Finkbeiner, D. P. 2011, ApJ, 737, 103
Seitenzahl, I. R., Ciaraldi-Schoolmann, F., Röpke, F. K., et al. 2013, MNRAS, 429, 1156
Seitenzahl, I. R., Taubenberger, S., & Sim, S. A. 2009, MNRaS, 400, 531
Seitenzahl, I. R., Timmes, F. X., & Magkotsios, G. 2014, ApJ, 792, 10
Shappee, B. J., Stanek, K. Z., Kochanek, C. S., & Garnavich, P. M. 2016, arXiv:1608.01155
Shen, K. J., & Schwab, J. 2017, ApJ, 834, 180
Sirianni, M., Jee, M. J., Benéz, N., et al. 2005, PASP, 117, 1049
Sollerman, J., Lindahl, J., Kozma, C., et al. 2004, A&A, 428, 555
Sparks, W. B., & Axon, D. J. 1999, PASP, 111, 1298
Srivastav, S., Ninan, J. P., Kumar, B., et al. 2016, MNRAS, 457, 1000
Stritzinger, M., & Sollerman, J. 2007, A&A, 470, L1
Sur, B., Norman, E. B., Lesko, K. T., Browne, E., & Larimer, R.-M. 1990, PhRvC, 42, 573
Swartz, D. A., & Wheeler, J. C. 1991, ApJL, 379, L13
Taubenberger, S., Elias-Rosa, N., Kerzendorf, W. E., et al. 2015, MNRAS, 448, L48
Truran, J. W., Arnett, W. D., & Cameron, A. G. W. 1967, CaJPh, 45, 2315
Woosley, S. E., Arnett, W. D., & Clayton, D. D. 1973, ApJS, 26, 231
Yang, Y., Wang, L., Baade, D., et al. 2017, ApJ, 834, 60
Zhang, K., Wang, X., Zhang, J., et al. 2016, ApJ, 820, 67
Zheng, W., Shivvers, I., Filippenko, A. V., et al. 2014, ApJL, 783, L24